

# Experimental evidence and numerical simulation of size effects on the ductile fracture of metallic materials

Alberto Carpinteri · Mauro Corrado  ·  
Baoming Gong · Pasquale Perdonò

Received: 12 September 2016 / Accepted: 8 March 2018 / Published online: 15 March 2018  
© Springer Science+Business Media B.V., part of Springer Nature 2018

**Abstract** The results of experimental tests investigating the size effects on single-edge-notched metallic specimens loaded in three-point bending are presented. Five different specimen scales were tested, with dimensions varying within the range 1:16. The samples were subjected to a fatigue pre-cracking to produce a sharp crack stemming from the notch root and, then, a quasi-static loading process was carried out up to the complete failure, in order to capture also the post-peak response. Notable size effects on the overall behaviour were obtained, with a variation of the failure mode from plastic collapse to ductile fracture and brittle failure by increasing the specimen size. An interpretation of the obtained size effects on ductile fracture is proposed based on numerical simulations carried out with a finite-element model that combines the cohesive method and the  $J_2$  plasticity to take into account all the possible mechanisms for energy dissipation. The best-fitting of the experimental results is obtained by scaling the mechanical properties with the specimen size, thus proving the need of considering size-dependent constitutive laws to correctly predict the ductile fracture.

Finally, scale-invariant cohesive properties are derived on the base of the fractal approach to the size effect.

**Keywords** Metals · Ductile fracture · Testing and modelling · Cohesive zone model · Plasticity · Size effects · Fractals

## 1 Introduction

Failure of metallic materials is a complex phenomenon that involves interplay between plasticity and fracture. Initial defects, such as microcracks, voids or inclusions, tend to be origins of internal cavity creation and growth under deformation. Furthermore, those microdefects may coalesce together into further material separation. Ductile fracture in metals usually consists of several micromechanical stages: first, the formation of necking (Fig. 1a) induces the micro-scale void or cavity nucleation from inclusions or second-phase precipitations (Fig. 1b), then enlargement or growth of those voids take place as the loading increases, and finally coalescence of voids (Fig. 1c) cause rapid propagation of cracks (Fig. 1d) and complete loss of material integrity (Fig. 1e).

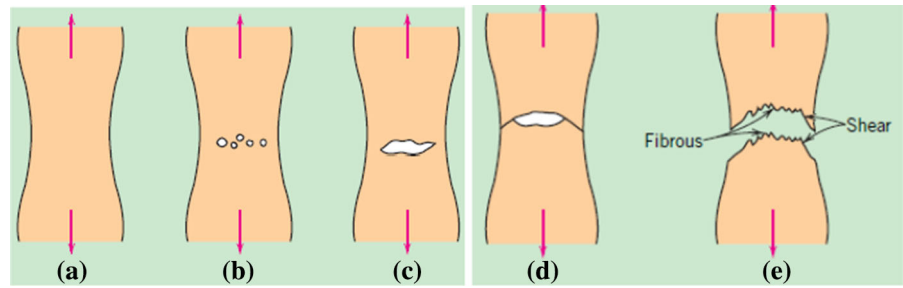
As far as the modelling point of view is concerned, various approaches were proposed for ductile fracture. The Gurson model is one of the most widely known models (Gurson 1975; Tvergaard and Needleman 1984; Zhang et al. 2000), and was derived from an approximate limit-analysis of a hollow sphere made of

---

A. Carpinteri · M. Corrado (✉) · P. Perdonò  
Department of Structural, Geotechnical and Building  
Engineering, Politecnico di Torino, Corso Duca degli  
Abruzzi 24, 10129 Torino, Italy  
e-mail: mauro.corrado@polito.it

B. Gong  
Department of Material Science and Engineering,  
Tianjin University, Road Weijin 92, Tianjin 300072, China

**Fig. 1** Different stages in ductile fracture failure: **a** initial necking, **b** small cavity formation, **c** coalescence of cavities to form a crack, **d** crack propagation, and **e** final shear fracture (Callister 2007)



ideally plastic material. Then, it was further improved by Tvergaard and Needleman (1984) accounting for the effect of coalescence to predict the void nucleation and growth. The path independent  $J$ -integral was also widely applied in ductile fracture. Essentially, it is an important parameter in nonlinear fracture mechanics and extends the application of linear elastic fracture mechanics to the nonlinear elastic behaviours, playing the role of  $K$  and  $G$  in characterizing the near crack tip region. Rice (1968) first applied it to fracture mechanics. However, the adopted constitutive stress-strain relationships are nonlinear elastic, differing from practical elastic-plastic ones. Even though they can have the same response under monotonically increasing load, they exhibit completely different performance when unloading and large scale yielding occur. In this sense, it may be more reasonable to define the  $J$ -integral as a nonlinear elastic fracture parameter than an elastic-plastic one. Moreover, it is now generally accepted that the  $J$ -integral resistance curves may be significantly influenced by the loading condition and the specimen size. Alternatively, the ductile crack growth resistance curve is presented in the form of the classical fracture mechanics parameters  $\Gamma$  (energy release rate  $G$ , path independent  $J$ -integral, or crack opening displacement  $\delta$ ) versus crack extension  $\Delta a$ : a crack starts to propagate at  $\Gamma = \Gamma_0$ , then grows in a stable manner with increasing  $\Gamma$ , and the resistance eventually reaches its steady-state value  $\Gamma_{ss}$ . Typically,  $\Gamma_{ss}$  is much larger than  $\Gamma_0$  and primarily comprises the additional irreversible contribution from remote and local plastic energy dissipation in the bulk (Anderson 1995). Unfortunately, the resistance curve cannot be considered as a material property due to its significant dependence on specimen size, initial crack length and loading configuration.

The cohesive zone model has been extensively used to study ductile fracture and ductile to brittle transition in the fracture of metallic materials (Chen et al. 2003;

Scheider and Brocks 2003; Cornec et al. 2003; Liu et al. 2013; Chakraborty and Biner 2014). One of the key issues in the application of this model is the choice of the material constitutive law within the cohesive zone. The traction-separation law is not known a priori and there is not an unequivocal correlation between the law and the result of the analysis. Therefore, different cohesive laws were proposed to describe different fracture processes. Tvergaard and Hutchinson (1992) discussed the applicability of the cohesive zone model to ductile fracture, where it was used only for the fracture process, whereas the finite plastic deformations outside the fracture zone—as well as necking in initially uncracked tensile specimens—were taken into account through  $J_2$  flow theory. Furthermore, Siegmund and Brocks (1999) and Banerjee and Manivasagam (2009) proposed cohesive zone models in which the peak stress and the cohesive energy are functions of the stress triaxiality. More in details, the peak stress increases whereas the cohesive energy decreases with triaxiality. The effectiveness of triaxiality dependent models has been proven by several studies investigating the effects of specimen size, initial crack extension, specimen geometry and loading conditions on the crack growth resistance behaviour (Siegmund and Brocks 2000; Rashid and Banerjee 2013). Finally, the triaxiality dependent approach has been extended by introducing rate-sensitive cohesive models to simulate the ductile crack growth under dynamic loading conditions (Anvari et al. 2006).

Recent contributions to the use of the cohesive methods concern the determination of the traction-separation law on micromechanical basis. To this aim, specific failure mechanisms such as, for instance, the ductile damage consisting of micro-void nucleation, growth and coalescence, are analysed at the micro-scale level and the deformation behaviour of the representative volume element is transferred to the cohesive inter-

face (Scheider 2009; Paggi et al. 2013; Yalcinkaya and Cocks 2015).

With reference to the ductile fracture in thin cracked metallic plates, a cohesive zone model was derived based on the stress and deformation analyses in the necking zone (Jin and Sun 2005). Similar to the Dugdale model (Dugdale 1960), the narrow necking zone (a localized deformation band) may be in fact idealized as a cohesive zone: the cohesive surface separation is approximated by the relative displacement of the upper and lower boundaries of the necking zone, whereas the cohesive traction is identified as the normal stress at the boundaries of the necking zone. As such, the cohesive energy in the cohesive zone model can be regarded as the energy stored and dissipated in the localization zone, which includes both the plastic dissipation in the bulk and the local dissipation due to the crack propagation. Following this idea, the hardening cohesive zone model was proposed by Carpinteri et al. (2012) for modelling ductile fracture. Its application to simulate compact tension tests on specimens with different dimensions proved its capability to capture the size effects on the overall mechanical response. In this context, the fractal geometry concepts that were introduced to elaborate the influence of the microstructural disorder typical of quasi-brittle materials (Carpinteri 1994; Carpinteri et al. 1995), giving rise to the so-called fractal cohesive crack model (Carpinteri et al. 2002), were retrieved to define a scale-independent hardening cohesive constitutive law.

In the present work, the effect of the structural size on the mechanical behaviour of notched metallic specimens subjected to bending is investigated by means of experimental tests on samples having different sizes scaled in the range 1:16, and simulated with a finite-element approach. From the conceptual and modelling standpoints, such a study is the extension to the problem of ductile fracture of the work carried out by Carpinteri and co-workers (Carpinteri 1994; Carpinteri et al. 2002) to analyze the size effect on the constitutive laws of quasi-brittle materials. Here, the ductile fracture is modeled with a numerical approach similar to those proposed by Tvergaard and Hutchinson (1992) and Siegmund and Brocks (1999), which combine the cohesive zone model used for crack propagation to plasticity for the bulk. The objective is twofold: first, to determine the size-dependent constitutive laws needed to capture, together with the coupling between cohesive zone model and plasticity, the com-

plex mechanical response associated to ductile fracture and, second, to derive scale-invariant material properties on the base of the fractal approach to size effect.

The manuscript is organized as follows. The results of the experimental tests are presented in Sect. 2, while the effects of the structural dimension on the material properties and the transition among different types of failure are discussed in Sect. 3. Then, the numerical model based on the finite-element method proposed to simulate the behaviour of the experimental tests that exhibited a ductile fracture is presented in Sect. 4. Such a model combines the cohesive zone model with the  $J_2$  plasticity to take into account all the possible mechanisms for energy dissipation involved in the considered cases. Finally, in Sect. 5 the obtained scale-effects on the mechanical properties are interpreted in the framework of the fractal approach to size effects, in order to determine scale-independent cohesive constitutive parameters.

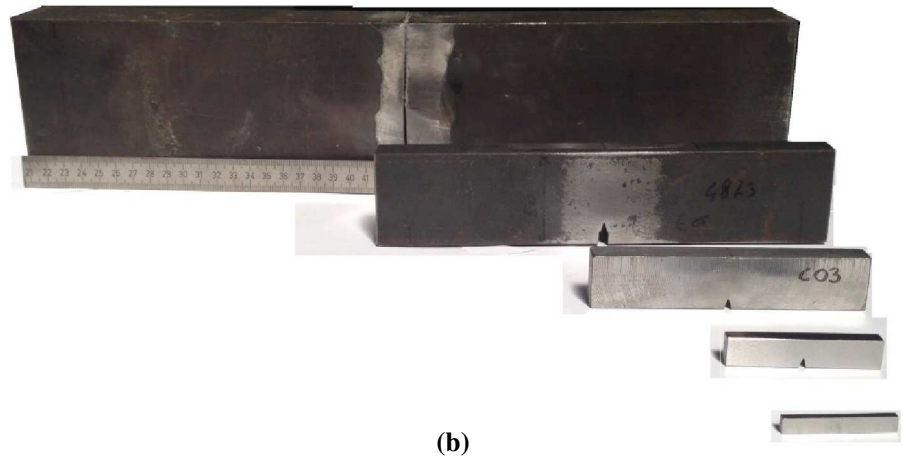
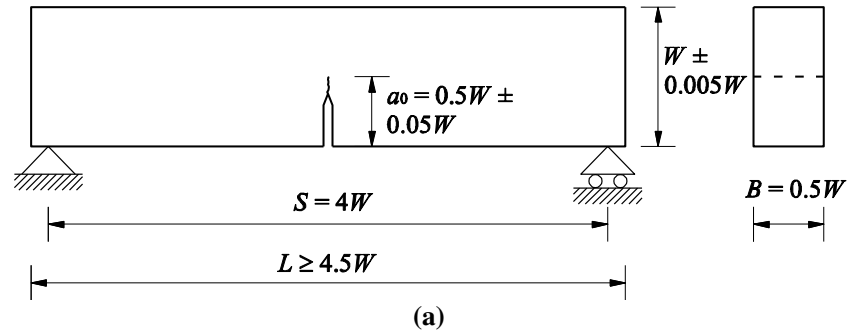
## 2 Experimental programme

Three-point bending (TPB) tests were performed on SENB specimens having five different sizes, scaled in the range 1:16. More in details, the depth,  $W$ , of the different series of beams is equal to 6.25, 12.5, 25, 50 and 100 mm. The span to depth ratio,  $S/W$ , and the thickness to depth ratio,  $B/W$ , were 4 and 0.5, respectively. The ratio between the initial crack length and the beam depth,  $a_0/W$ , was equal to  $0.5 \pm 0.05$  (see the sketch in Fig. 2a for the definition of the geometrical parameters). Three specimens were tested per each series, for a total of 15 samples. The geometrical parameters of the five scales are reported in Table 1. As it can be evinced from the table, the specimens are identified by means of a code representative of the specimen size, varying from S1 for the smallest scale to S16 for the largest one, followed by a number from 1 to 3 identifying the specific specimen inside the group. A picture of the samples, evidencing the extension of the scale range analysed, is shown in Fig. 2b.

### 2.1 Material characterization

In the present experimental programme, C40 steel was used, which is a non-alloy steel for quenching and tempering, as defined by EN 10083-2 (2006). Such a steel is largely used to produce equipment and devices for

**Fig. 2** Three-point bending test specimens: **a** definition of the geometrical parameters; **b** picture of the five specimen scales

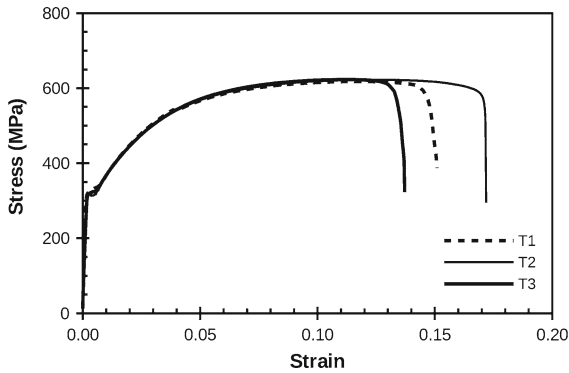


**Table 1** Geometrical parameters of the specimens

Specimen	$W$ (mm)	$B$ (mm)	$L$ (mm)	$S$ (mm)	Notch + fatigue crack $a_0$ (mm)	$a_0/W$
S1-1	6.25	3.12	40	25	3.2	0.51
S1-2					3.3	0.53
S1-3					2.9	0.46
S2-1	12.50	6.25	65	50	6.5	0.52
S2-2					6.3	0.50
S2-3					6.3	0.50
S4-1	25	12.50	120	100	13.8	0.55
S4-2					12.7	0.51
S4-3					11.5	0.46
S8-1	50	25	230	200	21.0	0.42
S8-2					25.7	0.51
S8-3					26.5	0.53
S16-1	100	50	450	400	51.2	0.51
S16-2					53.4	0.53
S16-3					52.3	0.52

**Table 2** Chemical composition of C40 steel (%)

C	Mn	Cr	Mo	Ni	Si	S	P
0.37–0.44	0.50–0.80	0.04	0.10	0.40	0.40	0.045 (max)	0.045 (max)

**Fig. 3** Stress versus strain constitutive law for steel C40 obtained from uniaxial tensile tests

mechanical applications. As concerns the heat treatment condition, the tested material is normalized (+ N). Its chemical composition is reported in Table 2. Tensile tests were performed on three rectangular tension test specimens with dimensions defined according to the ASTM E 8/E 8M (2008). In particular, the cross section of the central part of the specimen, the one interested by yielding and rupture, is  $10 \times 10 \text{ mm}^2$ . The stress versus strain curves obtained from the tensile tests are shown in Fig. 3. The average values of the mechanical properties are: yielding strength,  $\sigma_y$ , equal to 322 MPa, ultimate strength,  $\sigma_u$ , equal to 624 MPa, and elastic modulus,  $E$ , equal to 205.7 GPa. The ultimate strain, referred to an initial base of measurement of 60 mm, is about 15%. The strain hardening exponent is between 0.11 and 0.16, and the strength coefficient is about 1100 MPa (Sonmez and Demir 2007).

## 2.2 Specimens preparation

All the tested specimens were prepared as recommended by the standards for the evaluation of the fracture toughness, namely BSI 7448 Part 1 (1991) and ASTM E 399-09 (2009). V-shaped notches having a depth of  $0.3W$  were produced with a cutter in the mid-span position. Then, a fatigue crack was developed from the tip of the notch to produce a total initial crack  $a_0$ , given by the sum of the initial notch and the fatigue crack, equal to  $0.5W$ . To this aim, each speci-

men was subjected to fatigue cycles in the TPB scheme, characterized by decreasing amplitudes as the crack propagated and approached the desired length. The maximum force was determined in order to keep the stress intensity factor at the crack tip below  $0.6 K_{Ic}$ . At that stage, an estimation of the material toughness was assumed, equal to  $50 \text{ MN/m}^{3/2}$ . During the fatigue tests, the crack length was monitored by means of optical methods. Then, its exact value was determined after the final test, on the post-mortem specimens. Due to the practical difficulties to perform fatigue tests on the specimens at the two smallest scales, S1 and S2, such samples were cut from specimens having dimensions of the sample S4, after the fatigue pre-cracking. The values of the total initial crack for all the specimens are reported in Table 1. As expected, the ratio  $a_0/W$  is not exactly 0.5, although its variation is within the range  $0.45W$  and  $0.55W$ , in accordance with the ASTM recommendations (ASTM E 399-09 2009).

## 2.3 Testing procedure

The specimens were tested in the TPB scheme. In order to have a high accuracy in the measurement of the applied force for all the specimen scales two different servo-hydraulic testing machines were used, with capacity of 100 and 1000 kN respectively, equipped with load cells having capacity of 10, 100 and 500 kN. Analogously, two frames with different dimensions were used to applied the load according to the TPB scheme. All the specimens were tested under displacement control: mid-span deflection control for the series S1 and S2, and crack mouth opening displacement (CMOD) control for the specimens S4, S8 and S16, for which a more brittle response was expected. At that purpose, the specimens belonging to the latter series were equipped with a clip-on gauge, as shown in Fig. 4. The same loading rate, defined as the increment of the mid-span deflection over time for specimens S1 and S2, and as the increment of CMOD over time for specimens S4, S8 and S16, was assumed for all the specimens belonging to the same series. In the case of brittle failure, the entire post-peak behaviour was detected,

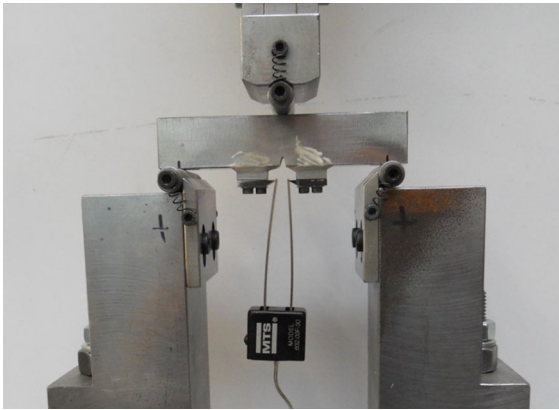


**Fig. 4** Experimental setup for the three-point bending tests (specimen S4)

up to complete separation of the specimen into two parts. On the contrary, in the case of plastic failure the tests were interrupted when the geometry was completely changed with respect to the TPB scheme due to large deformations, much before the final collapse was reached. For each test, time, load, mid-span deflection and CMOD were recorded.

#### 2.4 Experimental results

From a qualitative point of view, different global responses were evidenced by varying the specimen size. In particular, the obtained failure mechanisms can be grouped into three main types: prevalent ductile behaviour, with a full development of a plastic hinge around the mid-span cross section (Fig. 5a, b); crack propagation with a concurrent development of limited plasticity, (Fig. 5c, d); and crack propagation with negligible plastic deformations (Fig. 5e, f). In the following, these three failure mechanisms will be referred to as plastic collapse, ductile fracture and brittle failure, respectively. Significant differences between the different types of failure can be also evidenced by comparing the ligament cross sections after failure. The picture in Fig. 6a shows the ligament cross section of the specimen S4-2, which exhibited a ductile fracture. In such a picture it is possible to clearly distinguish the three different parts of the crack, namely the initial machined notch, the fatigue crack, and the quasi-static crack. In particular, it is also possible to see the effect of plasticity, which gave rise to the development of a permanent transversal contraction of the cross section in corre-

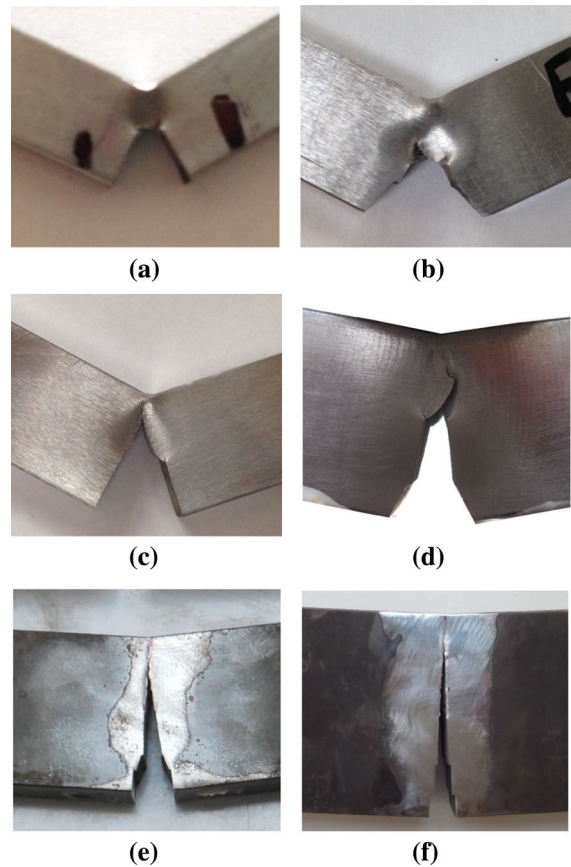


**Fig. 5** Pictures representative of the three different types of failure obtained: **a** and **b** plastic collapse, with full development of a plastic hinge in specimens S1-2 and S2-3; **c** and **d** crack propagation coupled to the development of limited plasticity in specimens S2-2 and S4-2; **e** and **f** brittle failure in specimens S8-1 and S16-1

spondence of the quasi-static crack. A similar picture is shown in Fig. 6b for the specimen S8-1, which was affected by a brittle failure. In this case, no evidences of plasticity are visible.

The load versus mid-span deflection curves obtained for the 15 tested specimens are shown in Fig. 7, grouped according to the specimen size. Two specimens out of three of the series S1, namely S1-1 and S1-3, exhibited a ductile fracture (Fig. 7a). In these cases, the initial elastic branch is followed by a hardening phase up to the peak load, after which a stable softening response in displacement control is obtained. The full load versus displacement curve was captured, up to the complete failure of the specimen. The peak load of specimen S1-3 is about 20% higher than that of S1-1. This is certainly due to a higher value of the ligament depth, as

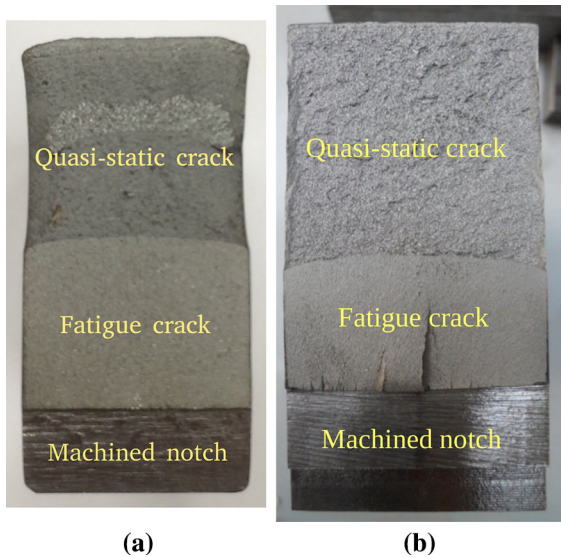


**Fig. 6** Ligament cross section after failure: **a** ductile fracture for specimen S4-2 with clear evidence of permanent transversal contractions, and **b** brittle failure for specimen S8-1 without evidences of plastic deformations

it can be evinced from Table 1. The post-peak softening branches are almost overlapped. On the contrary, a plastic collapse occurred in the sample S1-2, determining a larger extension of the hardening phase and a lower slope of the post-peak branch compared to the two previous cases. The test was interrupted when the geometry was completely changed with respect to the TPB scheme due to large deformations, much before the final collapse was reached. Analogous results were obtained for the series S2: ductile fracture for specimens S2-1 and S2-2, and plastic collapse for specimen S2-3 (Fig. 7b). The experimental results of the series S4 are shown in Fig. 7c. In this case, two specimens exhibited plastic collapse, namely S4-1 and S4-3, whereas only the sample S4-2 was characterized by ductile fracture. The dimension of the specimens S4 was large enough to equip them with a clip-on gauge in order to measure the CMOD during the test. Therefore, their loading process was controlled by the crack opening instead of the mid-span deflection. As in the previous cases, the tests of the specimens S4-1 and S4-3 were interrupted due to a broad variation in the geometry that led to a loss in representativeness of the results. On the contrary, the post-peak behaviour of the sample characterized by ductile fracture, S4-2, was fully captured. Differently from specimens S1 and S2, in this

case some local instabilities appeared during the post-peak phase. They evidence a very brittle behaviour of the specimen, that was not possible to prevent even by controlling the test by means of the CMOD. Such instabilities were usually anticipated by the accumulation of plastic deformations ahead of the crack tip. Then, when a certain value of crack tip opening displacement was reached, the crack propagated suddenly for a finite length, with a concomitant release of a large amount of energy. After this drop, the load capacity was recovered and the loading process continued with a stable crack propagation. Such a behaviour was even more evident in specimens S8 and S16, for which the load versus displacement curves are shown in Fig. 7d, e. All the specimens having such dimensions were characterized by a brittle failure. An almost linear-elastic response was obtained up to the peak-load, followed by an unstable crack propagation. The process was highly unstable and impossible to be controlled, even by means of the CMOD control. Therefore, the vertical drops in the load-displacement diagrams do not represent the real behaviour of the specimen, since they are consequent to the loss of control of the test. The post-peak phase is characterized by a step-wise crack propagation alternated to the development of limited plastic deformations, represented by horizontal plateaus in the load-displacement diagrams. All the specimens S8 and S16 were tested up to complete failure.

### 3 Size effects on the fracture toughness and the mechanical response

As evidenced by the experimental results presented in the previous section, very different overall mechanical behaviours were obtained by varying the specimen size. In general, the global trend evidences a transition from ductile to brittle response by increasing the specimen size. A high brittleness characterizes the behaviour of specimens with a depth larger than or equal to 50 mm. Usually, metallic materials are expected to show such a brittle response only at larger scales. However, the considered steel, namely C40, has a high content of carbon that is at the origin of such a brittleness. On the contrary, a high variability in the mechanical response was obtained for the specimens with depth in the range between 6.25 and 25 mm. Probably, such a range represents the transition between brittle and ductile behaviour for the con-

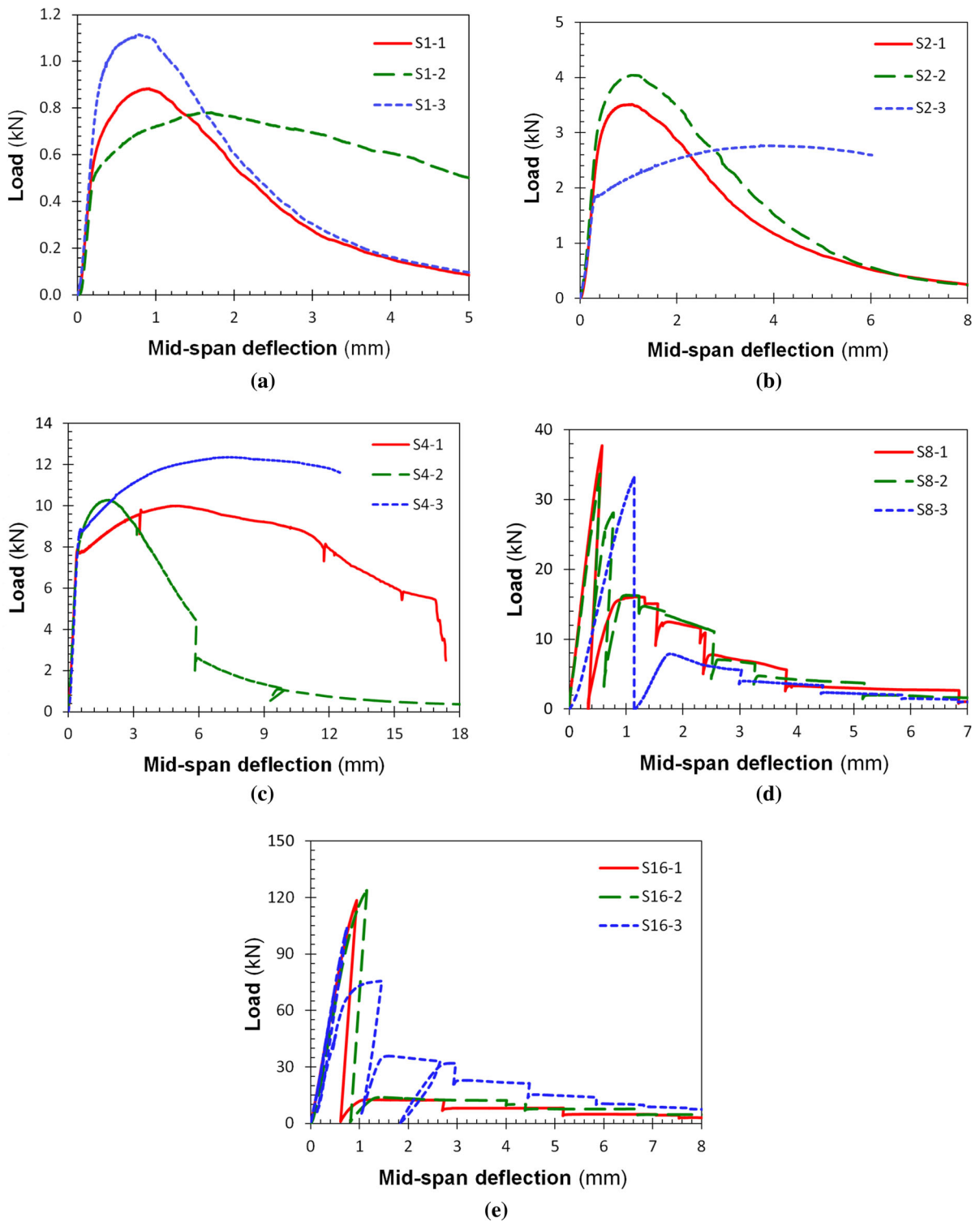


**Fig. 7** Experimental load versus displacement curves for the five different specimen sizes. **a**  $W = 6.25$  mm. **b**  $W = 12.50$  mm. **c**  $W = 25$  mm. **d**  $W = 50$  mm. **e**  $W = 100$  mm

**Table 3** Fracture toughness obtained from the experiments

Specimen	W (mm)	$K_{Ic}^*$ (MN/m <sup>3/2</sup> )	$K_{Ic,5}$ (MN/m <sup>3/2</sup> )
S1-1	6.25	39.17	22.25
S1-2		37.08	21.12
S1-3		42.08	32.52
S2-1	12.50	57.00	42.34
S2-2		61.81	44.81
S2-3		42.50	27.82
S4-1	25	64.24	51.39
S4-2		57.56	40.96
S4-3		58.11	38.58
S8-1	50	56.20	56.20
S8-2		66.86	67.24
S8-3		69.68	67.37
S16-1	100	83.42	71.11
S16-2		93.56	81.49
S16-3		82.88	76.32

sidered material and, therefore, the obtained variations have to be attributed to statistical reasons. A plastic collapse is expected for specimens with depth lower than 6 mm. The analysis of the size effects is herein carried out from a quantitative point of view, through the evaluation of the material toughness.

The material toughness, represented by the parameter  $K_{Ic}$ , was evaluated for all the considered scales. Obviously, the values obtained from specimens S1, S2 and S4, cannot be considered as the true material toughness, since not negligible plastic deformations occurred in the pre-peak phase. Such a parameter is a function of the load by means of the following expression, which holds for the TPB scheme:

$$K_Q = \frac{P_Q S}{B W^{3/2}} f\left(\frac{a}{W}\right), \tag{1}$$

where  $K_Q$  is the estimated value for the material toughness,  $P_Q$  is a value of the load taken from the load-displacement curve,  $B$ ,  $W$  and  $S$  are the thickness, the depth and the span of the specimen, and  $f(a/W)$  is a specific shape function that can be taken from fracture mechanics handbooks (Tada et al. 1963). Two different values are calculated to identify the material toughness: the fictitious toughness  $K_{Ic}^*$ , which is evaluated with reference to the peak load ( $P_Q = P_{peak}$ ), and the parameter  $K_{Ic,5}$ , which is evaluated according to the

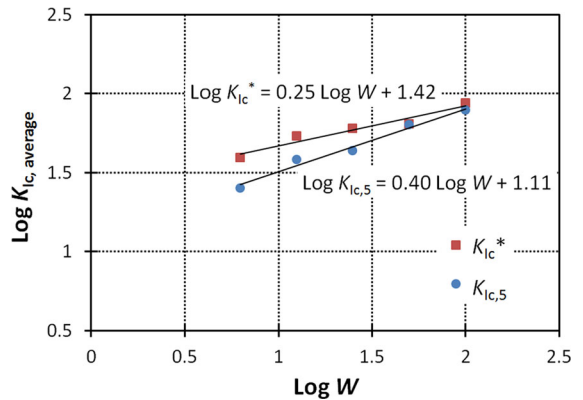


**Fig. 8** Size effects on the fracture toughness

procedure provided by the ASTM recommendations (ASTM E 399-09 2009). In the latter case, the load is identified by drawing a line in the load-displacement diagram having a slope reduced by 5% with respect to the initial tangential stiffness. The results obtained for all the tested specimens are reported in Table 3, whereas the average values for each specimen series are shown in the bi-logarithmic diagram in Fig. 8, as a function of the beam depth. The square markers refer to  $K_{Ic}^*$ , whereas the circles to  $K_{Ic,5}$ . As expected, a significant difference between the two values is obtained for specimens S1, S2 and S4, due to a large difference between the load corresponding to the end of the elas-

tic phase and the peak load. On the contrary, the two parameters have very similar values for samples S8 and S16. Both the evaluated parameters increase by increasing the specimen size according to linear functions in the bi-logarithmic diagram (the fitting equations are reported in Fig. 8).

Based on the values of the fracture toughness obtained for the different scales, a normalization of the experimental curves is now pursued, in order to easily compare them in a single diagram. The correct normalization can be obtained by applying the Dimensional Analysis, based on the Buckingham's Theorem (see Carpinteri 1982; Corrado et al. 2011 for examples of its application to fracture mechanics problems). For the considered problem, the load  $P$  can be normalized with respect to the fracture toughness and the specimen depth and thickness, whereas the mid-span deflection  $\delta$  can be normalized with respect to the specimen depth, as follow:

$$\tilde{P} = \frac{P}{K_{Ic} W^{0.5} B} \quad (2)$$

$$\tilde{\delta} = \frac{\delta}{W} \quad (3)$$

A representative curve for each specimen series is shown in dimensionless form in Fig. 9. Each curve is normalized with respect to the average value of the fracture toughness corresponding to its size. In particular, the parameter  $K_{Ic,5}$  is used. The obtained diagram pinpoints the general ductile-to-brittle transition occurring by increasing the specimen size. More in details, a limited transition in the range of the normal softening behaviour is obtained starting from specimen S1 and doubling and quadrupling the dimensions, whereas a jump from normal softening to snap-back instability (softening branch with positive slope) is obtained by doubling the dimensions from specimen S4 to specimen S8. Then, a further increase in the brittleness is obtained from sample S8 to S16. Actually, the portion of the load-displacement curve corresponding to the snap-back branches was not captured since it was not possible to control the unstable behaviour. However, such branches can be guessed, as done in Fig. 9b with a dashed line connecting the pre-peak with the post-peak phases. From the diagrams in Fig. 9a it is evident that specimens with dimensions intermediate between S4 and S8 should be tested to get a smoother transition from ductile to brittle behaviour.

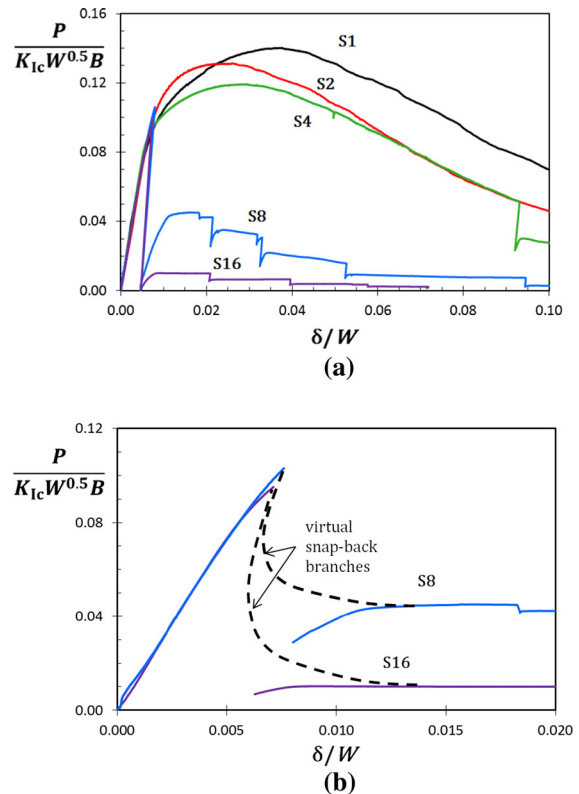


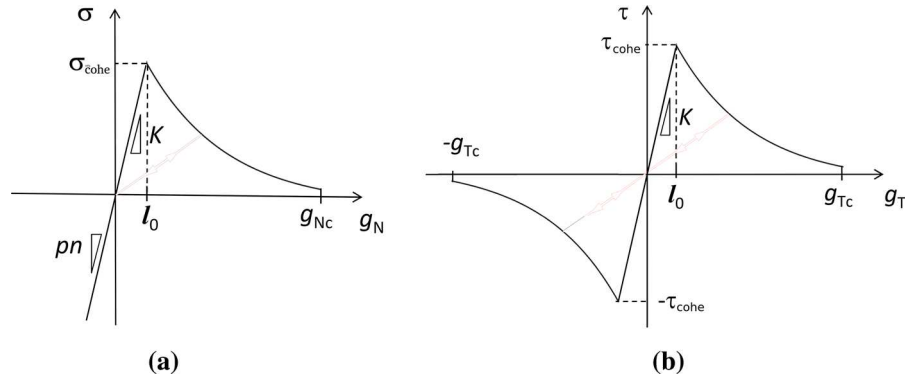
**Fig. 9** **a** Dimensionless load versus displacement curves for the five different specimen sizes; **b** magnification of a portion of the curves referred to specimens S8 and S16 with the drawing of the uncaptured snap-back branches

#### 4 Numerical modelling

In the present section, the numerical model based on the finite-element method used to simulate the macro-scale response of the TPB tests is presented. In particular, focus was on the specimens characterised by ductile fracture, namely S1-1, S1-3, S2-1, S2-2 and S4-2. In the case of plastic collapse, in fact, plasticity can give good predictions for the ultimate load-carrying capacity, whereas in the case of brittle behaviour (specimens S8 and S16), linear elastic fracture mechanics is the appropriate model to be applied.

The mechanical behaviour of the set of specimens herein considered was characterized by an interplay between fracture and plasticity. Therefore, in spite of the fact that the material is homogeneous, two different constitutive models were used to model material damage and energy dissipation: the cohesive zone model (CZM) for the macroscopic crack propagat-

**Fig. 10** Cohesive zone model formulation for irreversible Mode I or Mode II cracking. **a** Mode I, **b** Mode II



ing in the mid-span cross section, and the elasto-plasticity for material damage in the bulk. Such an approach, which combines two basic forms of non-linearity, was successfully applied by the authors in meso-scale finite-element simulations, in which the polygrain microstructure of metals was explicitly modelled (Paggi et al. 2013; Corrado et al. 2014). In that case, elasto-plasticity was used to model the material behaviour inside the grains whereas the CZM was adopted for intergranular cracking. The interplay between these two models led to homogenized macro-scale stress versus relative displacement relations characterized by an almost linear initial branch followed by a plastic hardening and finally by a softening phase. Moreover, by changing the ratio between the peak cohesive stress and the yielding stress of the plastic law, a transition from ductile to brittle response was predicted.

#### 4.1 Constitutive models

The steel was modelled as an elastic-plastic material with isotropic hardening. The  $J_2$  model was used, having the Young’s modulus,  $E$ , the Poisson ratio,  $\nu$ , the initial uniaxial yield stress,  $\sigma_y$ , and the isotropic hardening modulus,  $H_{iso}$ , as input parameters. In order to simulate the discrete crack propagation and localized plastic phenomena a cohesive constitutive law was introduced, whose shape is characterized by a linear ascending branch followed by an exponential softening. A formulation for mixed mode crack propagation, i.e. with coupling between normal and tangential cohesive tractions, was used. It is expressed by the following equations:

$$\sigma = \begin{cases} \sigma_{\max} \exp\left(\frac{-l_0 - |g_T|}{R}\right) \frac{g_N}{l_0}, & \text{if } 0 \leq \frac{g_N}{R} < \frac{l_0}{R}, \\ \sigma_{\max} \exp\left(\frac{-g_N - |g_T|}{R}\right), & \text{if } \frac{l_0}{R} \leq \frac{g_N}{R} < \frac{g_{Nc}}{R}, \\ 0, & \text{if } \frac{g_N}{R} \geq \frac{g_{Nc}}{R}, \end{cases} \quad (4)$$

$$\tau = \begin{cases} \tau_{\max} \exp\left(\frac{-l_0 - g_N}{R}\right) \frac{g_T}{l_0}, & \text{if } 0 \leq \frac{|g_T|}{R} < \frac{l_0}{R}, \\ \tau_{\max} \operatorname{sgn}(g_T) \exp\left(\frac{-g_N - |g_T|}{R}\right), & \text{if } \frac{l_0}{R} \leq \frac{|g_T|}{R} < \frac{g_{Tc}}{R}, \\ 0, & \text{if } \frac{|g_T|}{R} \geq \frac{g_{Tc}}{R}, \end{cases} \quad (5)$$

where  $g_N$  and  $g_T$  are the relative opening and sliding displacements of the crack. A graphical representation of the pure Mode I and Mode II CZM relations is provided in Fig. 10. In the present model, the selection of the initial stiffness is made by varying the internal parameter  $l_0$ , which defines the opening and sliding displacements corresponding to the peak CZM tractions before the onset of the exponential softening. Such a stiffness has to be as high as possible to limit the introduction of fictitious compliances in the overall mechanical response of the beam. The parameter  $\sigma_{\max}$  in Eq. (4) is the maximum tensile cohesive traction, achievable in the limit case of  $l_0 = 0$ . On the contrary, the real peak value of the CZM law is  $\sigma_{cohe} = \sigma_{\max} \exp(-l_0/R)$ . The same is for the tangential component. The other parameters entering the formulation in Eqs. (4) and (5) are the critical opening and sliding displacements,  $g_{Nc}$  and  $g_{Tc}$ , corresponding to complete cracking in pure Mode I and Mode II loading, and the root mean square of the heights of the microscopically rough crack profile,  $R$ , (see Ciavarella et al. 2008 for the terminology). As compared to other CZM formulations (Tvergaard 1990; Xu and Needleman 1994) defining the cohesive tractions by a single nonlinear equation over the whole separation range, easier to be numerically imple-

mented, here the ascending branch is treated separately from the softening one. This choice allows us to change the cohesive fracture energy and the peak stress (acting on  $g_{Nc}$  and  $R$ ), keeping constant the initial stiffness, which is not always possible with other CZM formulations where a change of the nonlinear initial stiffness modifies the fracture energy as well. In compression, a penalty formulation was used, with a penalty parameter  $p_n$  a few order of magnitudes higher than the stiffness in tension.

#### 4.2 Finite-element model

A plane strain finite-element model was used to simulate the TPB tests. Due to the symmetry of the problem, only half of the beam was modelled, as shown in Fig. 11. The mesh consisted of quadrangular elements with linear shape functions for the bulk and a row of four nodes linear interface finite elements placed in the mid-span cross section, along the initial ligament. The interface elements have zero-thickness, as it is commonly used for the CZM (more details on the implementation of the cohesive method within the finite-element framework can be found in Paggi and Wriggers 2011; Corrado and Paggi 2015). The beam was simply supported in the bottom right corner node, whereas symmetry constraints were defined in the mid-span cross section (see Fig. 11). In the simulations, the loading process was displacement-controlled, i.e., a step-by-step increasing vertical displacement was imposed on the upper side of the mid-span cross section (point A in Fig. 11).

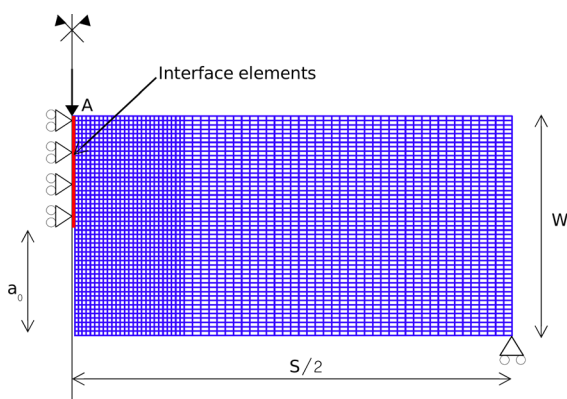


**Fig. 11** Finite element model used to simulate the experimental tests

The element size was selected in order to have a mesh fine enough to accurately resolve the process zone associated to the CZM. A commonly accepted rule is that at least four interface elements are included in the process zone. At that purpose, the length of the cohesive zone was estimated with the formula provided by Rice (Rice 1980) for plane strain conditions in statics:

$$l = \frac{9\pi}{32} \left( \frac{E}{1-\nu^2} \right) \frac{G_F}{\sigma_{cohe}^2} \quad (6)$$

where  $E$  is the Young's modulus,  $\nu$  is the Poisson ratio,  $G_F$  is the fracture energy, and  $\sigma_{cohe}$  is the cohesive strength. All the three simulated beams were meshed with 50 elements along the depth. Therefore, the element size was proportional to the beam size. It was 0.125 mm for specimen S1, 0.25 mm for specimen S2, and 0.5 mm for specimen S4. In all the three cases the element size was at least two order of magnitudes lower than the length of the cohesive zone (the estimated values for the cohesive length are given in Sect. 5, where the material properties used for the three specimen scales are reported).

Quasi-static loading conditions were assumed for the numerical simulations. The implicit solution scheme with the Newton–Raphson iterative method was adopted to solve the non-linear set of algebraic equations representing the mechanical problem. The simulations were run on the finite element code FEAP (Zienkiewicz and Taylor 2000).

### 5 Results and discussion

Following the experimental evidences of size effects on the mechanical properties pinpointed in Sect. 3, the fracture energy and the cohesive strength characterizing the CZM law and the initial yield stress of the elastic-plastic relationship were varied in the numerical simulations with the size of the specimen. At this regard, it is worth noting that a size dependency of the yielding and ultimate strength of metallic materials is well known in the literature (Richards 1954; Morquio and Riera 2004), and also recognized by Standards (EN 10277-2 2008).

For the considered specimens, S1-1, S1-3, S2-1, S2-2 and S4-2, the total dissipated energy was directly evaluated as the area beneath the load-displacement curves shown in Fig. 7a–c. The average values are:  $E_{diss} = 2360$  Nmm for  $W = 6.25$  mm,  $E_{diss} = 13440$  Nmm

**Table 4** Mechanical properties used for the numerical simulations

Sample	Cohesive law						Elastic–plastic	
	$\sigma_{\max}$ (MPa)	$l_0$ (mm)	$g_{Nc}$ (mm)	$R$ (mm)	$\sigma_{\text{cohe}}$ (MPa)	$G_F$ (N/mm)	$\sigma_y$ (MPa)	$H_{\text{iso}}$ (MPa)
S1	1000	0.050	0.70	0.18	757	152	600	3000
S2	900	0.065	0.85	0.25	694	188	550	3000
S4	600	0.070	1.10	0.45	514	225	380	3000

for  $W = 12.5$  mm, and  $E_{\text{diss}} = 58380$  Nmm for  $W = 25.0$  mm. Then, in the simplified hypothesis that the entire energy is dissipated by the crack propagation, a reference value for the fracture energy was determined by dividing the total dissipated energy by the area of the ligament. The average values obtained are:  $G_{F,\text{ref}} = 234$  N/mm for  $W = 6.25$  mm,  $G_{F,\text{ref}} = 350$  N/mm for  $W = 12.5$  mm, and  $G_{F,\text{ref}} = 381$  N/mm for  $W = 25$  mm. However, even though the considered cases showed a prevalent cracking mode, the plastic behaviour of the bulk material also contributed to dissipate energy. Therefore, the aforementioned reference values have to be intended as a rough, upper limit, estimate for the fracture energy to be adopted for the cohesive laws.

The free parameters that were adjusted to optimize the comparison between the numerical predictions and the experimental results were the cohesive strength,  $\sigma_{\text{cohe}}$ , and the fracture energy,  $G_F$ , for the cohesive model, and the initial yield stress  $\sigma_y$  for the elastic-plastic law. For each beam size, repeated simulations were run by varying the values of these three parameters until the numerical predictions best fitted the experimental results. Such a procedure led to the definition of the mechanical properties reported in Table 4 for the three beam scales. The corresponding cohesive and elastic-plastic constitutive laws are shown in Figs. 12 and 13, respectively. As regards the cohesive model, only the Mode I law is shown, since in the TPB test the contribution of Mode II to crack propagation is negligible. Following the trends evidenced by the experiments of the present study, the cohesive strength was decreased by increasing the specimen size, whereas the fracture energy was increased. Correspondingly, the critical opening,  $g_{Nc}$ , was increased with the scale. Based on the mechanical properties listed in Table 4, the following lengths of the cohesive zone are given by Eq. (6):  $l = 52$  mm for  $W = 6.25$  mm,  $l = 78$  mm for  $W = 12.5$  mm, and  $l = 170$  mm for  $W = 25.0$  mm.

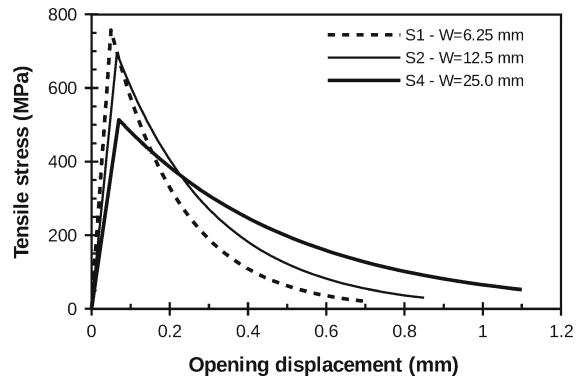


**Fig. 12** Scale-dependent cohesive laws adopted for the three specimen scales S1, S2 and S4

Such values confirm that the size of the finite elements was appropriate. As far as the elastic-plastic law is concerned, the initial yield stress was increased by increasing the beam size, whereas the isotropic hardening modulus was kept constant. It is worth noting that the elastic-plastic law for the specimen S4 matches quite well the stress-strain curve obtained from the uniaxial tensile tests carried out to characterize the tested material (grey curve in Fig. 13). This is fully consistent with the fact that the ligament cross section of the sample S4 ( $12.5 \times 12.5$  mm<sup>2</sup>) is very close to the cross section of the tensile test specimens ( $10 \times 10$  mm<sup>2</sup>).

As expected, the values of the fracture energy associated to the CZM laws used in the simulations are lower than the corresponding reference values computed in the hypothesis of energy entirely dissipated by crack propagation, and reported above. The difference between these two values is a measure of the amount of energy that is dissipated in the bulk by plasticity. In particular, the analysis of these data reveals that about 60% of the total energy is dissipated by the crack propagation and 40% by plasticity. This result is fully consistent with the experimental observation of limited permanent deformations in the volume (see Fig. 5c, d).

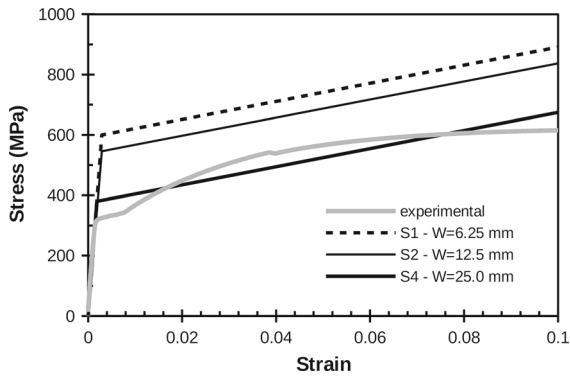
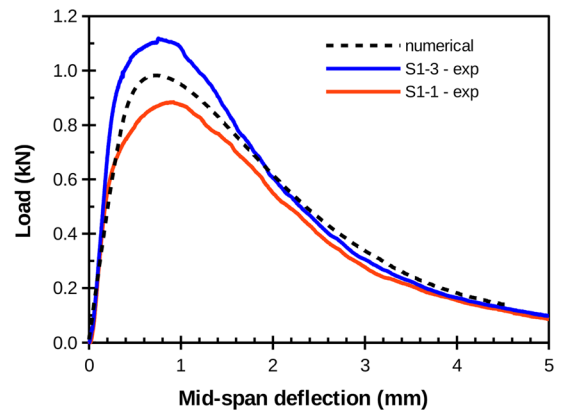


**Fig. 13** Scale-dependent elastic-plastic laws adopted for the three specimen scales S1, S2 and S4

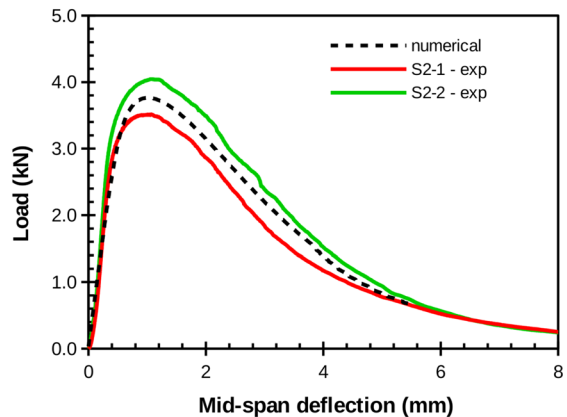
The load versus mid-span deflection curves obtained from the numerical simulations are shown in Fig. 14, where they are compared to the corresponding experimental curves. In all three cases, the numerical predictions match pretty well the experimental data. For specimens S1 and S2 the material properties were tuned in order to obtain an average behaviour with respect to the experimental curves.

The variation of the cohesive properties with the specimen scale can be interpreted in the framework of the fractal approach to size effects, proposed and discussed widely by Carpinteri (1994) and Carpinteri et al. (1995, 2002) for quasi-brittle materials, and recently extended also to metals (Carpinteri et al. 2012).

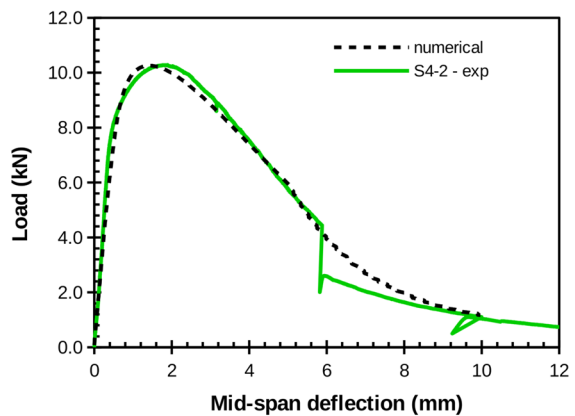
In this context, the nominal parameters of the cohesive law, namely  $\sigma_{\text{cohe}}$ ,  $g_{Nc}$  and  $G_F$ , are not assumed as material properties, as they depend on the resolution used to measure the domains where stress, strain and energy dissipation are defined. In particular, in the limit of a very high measure resolution, the stress and the strain tend to infinite, whereas the dissipated energy tends to zero. Finite values can be obtained only introducing fractal quantities, i.e., mechanical properties with non-integer physical dimensions. More specifically, the scaling of the cohesive strength  $\sigma_{\text{cohe}}$  is a consequence of the lacunarity of the ligament, the scaling of the fracture energy  $G_F$  is explained by the invasive fractality of the rough crack surface where energy dissipates, and the scaling of the critical displacement  $g_{Nc}$  can be explained by the fractal strain localization. In formulae, these scale-dependences are described by the following power-laws (for more details refer to Carpinteri et al. 2002):



(a)



(b)



(c)

**Fig. 14** Comparison between experimental results and numerical simulations for specimens S1, S2 and S4. **a**  $W = 6.25$  mm. **b**  $W = 12.5$  mm. **c**  $W = 25.0$  mm

$$\sigma_{cohe} = \sigma_{cohe}^* W^{-d_\sigma}, \tag{7a}$$

$$G_F = G_F^* W^{d_G}, \tag{7b}$$

$$g_{Nc} = \varepsilon_{Nc}^* W^{(1-d_\varepsilon)}, \tag{7c}$$

where  $\sigma_{cohe}^*$ ,  $G_F^*$  and  $\varepsilon_{Nc}^*$  are the true scale-invariant parameters, having anomalous physical dimensions, and  $W$  is the representative specimen dimension. In general, the exponents  $d_\sigma$  and  $d_G$  can be evaluated from the scale-dependent values of  $\sigma_{cohe}$  and  $G_F$ . In particular, they represent the slope, in the bi-logarithmic diagram, of the straight lines interpolating the values of  $\sigma_{cohe}$  and  $G_F$ , respectively, as functions of the specimen size. Such diagrams, build with the cohesive parameters used for the numerical simulations, are shown in Fig. 15. The interpolating straight lines give a value of 0.28 for both the exponents. Accordingly, the cohesive energy is dissipated over a domain having a physical dimension equal to  $2 + d_G = 2.28$ , which is a consequence of the roughness of the crack surface, whereas the ligament has a physical dimension equal to  $2 - d_\sigma = 1.72$  because of the presence of voids and defects (Carpinteri et al. 2002). As concerns the exponent  $d_\varepsilon$ , it can be obtained by applying the following relationship derived from the integral definition of the fractal fracture energy (see Carpinteri et al. 2002 for more details):

$$d_\sigma + d_G + d_\varepsilon = 1. \tag{8}$$

According to the fractal concepts herein outlined, it is possible to derive the scale-independent cohesive parameters  $\sigma_{cohe}^*$ ,  $\varepsilon_{Nc}^*$  and  $G_F^*$ , which are determined as the intercepts of the scaling-laws defined by Eq. (7). They assume the following values:  $G_F^* = 91.2 \text{ N/mm}^{1.28}$ ,  $\sigma_{cohe}^* = 1318 \text{ N/mm}^{1.72}$ ,  $\varepsilon_{Nc}^* = 0.23 \text{ mm/mm}^{0.56}$  (the physical dimension of the fractal strain is defined by  $d_\varepsilon$  that, according to Eq. (8), is equal to 0.44). Such fractal parameters represent the true material properties, independent of the structural scale.

### 6 Conclusions

In the present study, size effects on metallic materials have been analysed, with reference to C40 steel SENB specimens loaded in three-point bending. To this aim, experimental tests were carried out on geometrically similar specimens having five different dimensions scaled in the range 1:16. Such tests, extended

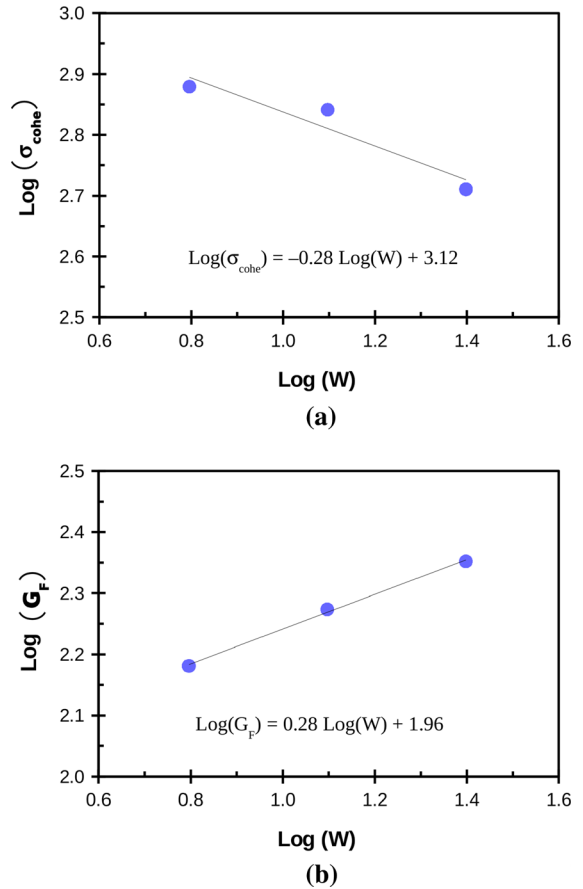


**Fig. 15** Size effects on the values of **a** the cohesive strength and **b** the fracture energy used for the numerical simulations

over a so wide range of sizes, represent an original and important contribution to the state-of-the-art, since the obtained results could serve as a benchmark for comparison with analytical and numerical models. A transition between three different failure mechanisms by increasing the specimen size was obtained: plastic collapse, with full development of a plastic hinge around the mid-span cross section; ductile fracture, with interplay between stable crack propagation and plasticity; and brittle failure, characterized by an unstable crack propagation without significant plastic deformations. The size dependency of the fracture toughness was also derived from the analysis of the experimental results. It was found to increase with the structural scale according to a power-law.

The mechanical response of the specimens that were characterized by a ductile fracture was simulated with a finite-element model that combines the CZM for the

crack propagation with an elastic-plastic behaviour for the bulk. The best-fitting of the experimental results was possible only by changing the mechanical properties of both the CZM and the elastic-plastic relation with the specimen size. Once more, this is a confirmation that, besides considering two different mechanisms of energy dissipation, namely crack propagation and plastic deformations, also the size effect has to be considered to correctly predict the behaviour of ductile fracture in metallic materials.

Moreover, a theoretical interpretation of the size effect on the cohesive law was done based on the fractal approach to size effect. On the one hand, such an approach leads to the definition of complex mechanical parameters having anomalous physical dimensions. On the other hand, it permits to derive the scale-invariant cohesive parameters for the considered material, that can be used to determine the scale-dependent constitutive laws for any given size.

## References

- Anderson TL (1995) Fracture mechanics: fundamentals and applications, 2nd edn. CRC Press, Boca Raton
- Anvari M, Scheider I, Thaulow C (2006) Simulation of dynamic ductile crack growth using strain-rate and triaxiality-dependent cohesive elements. *Eng Fract Mech* 73:2210–2228
- American Society for Testing and Materials (2008) ASTM E 8/E 8M-08 standard test methods for tension testing of metallic materials
- American Society for Testing and Materials (2009) ASTM E 399-09 standard test method for linear-elastic plane-strain fracture toughness  $K_{Ic}$  of metallic materials
- Banerjee A, Manivasagam R (2009) Triaxiality dependent cohesive zone model. *Eng Fract Mech* 76:1761–1770
- British Standards Institution (1991) BSI 7448-I Fracture mechanics toughness tests—Part 1: method for determination of  $K_{Ic}$ , critical CTOD and critical J values of metallic materials
- Callister WD (2007) Materials science and engineering: an introduction, 7th edn. Wiley, New York
- Carpinteri A (1982) Notch sensitivity in fracture testing of aggregative materials. *Eng Fract Mech* 16:467–481
- Carpinteri A (1994) Scaling laws and renormalization groups for strength and toughness of disordered materials. *Int J Solids Struct* 31:291–302
- Carpinteri A, Chiaia B, Ferro G (1995) Size effects on nominal tensile strength of concrete structures: multifractality of material ligaments and dimensional transition from order to disorder. *Mater Struct* 28:311–317
- Carpinteri A, Chiaia B, Cornetti P (2002) A scale-invariant cohesive crack model for quasi-brittle materials. *Eng Fract Mech* 69:207–217
- Carpinteri A, Gong B, Corrado M (2012) Hardening cohesive/overlapping zone model for metallic materials: the size-scale independent constitutive law. *Eng Fract Mech* 82:29–45
- Chakraborty P, Biner SB (2014) A unified cohesive zone approach to model the ductile to brittle transition of fracture toughness in reactor pressure vessel steels. *Eng Fract Mech* 131:194–209
- Chen CR, Kolednik O, Scheider I, Siegmund T, Tatzchl A, Fischer FD (2003) On the determination of the cohesive zone parameters for the modeling of micro-ductile crack growth in thick specimens. *Int J Fract* 120:517–536
- Ciavarella M, Greenwood JA, Paggi M (2008) Inclusion of interaction in the Greenwood & Williamson contact theory. *Wear* 265:729–734
- Cornec A, Scheider I, Schwalbe K-H (2003) On the practical application of the cohesive model. *Eng Fract Mech* 70:1963–1987
- Corrado M, Cadamuro E, Carpinteri A (2011) Dimensional analysis approach to study snap back-to-softening-to-ductile transitions in lightly reinforced quasi-brittle materials. *Int J Fract* 172:53–63
- Corrado M, Paggi M (2015) Nonlinear fracture dynamics of laminates with finite thickness adhesives. *Mech Mater* 80:183–192
- Corrado M, Paggi M, Carpinteri A (2014) A multi-scale numerical method for the study of size-scale effects in ductile fracture. *Metals* 4:428–444
- Dugdale DS (1960) Yielding of steel sheets containing slits. *J Mech Phys Solids* 8:100–114
- EN 10277-2 (2008) Bright steel products—Technical delivery conditions—Part 2: steels for general engineering purposes. European Committee for Standardization
- EN 10083-2 (2006) Steels for quenching and tempering—Technical delivery conditions for non alloy steels. European Committee for Standardization
- Gurson AL (1975) Plastic flow and fracture behaviour of ductile materials incorporating void nucleation, growth and coalescence, Ph.D. Thesis, Brown University
- Jin Z-H, Sun CT (2005) Cohesive fracture model based on necking. *Int J Fract* 134:91–108
- Liu J, Li J, Liu L (2013) Finite element analysis for brittle and ductile fracture using a unified cohesive zone model. *Adv Mech Eng* 5:924070
- Morquio A, Riera JD (2004) Size and strain rate effects in steel structures. *Eng Struct* 26:669–679
- Paggi M, Lehmann E, Weber C, Carpinteri A, Wriggers P, Schaper M (2013) A numerical investigation of the interplay between cohesive cracking and plasticity in polycrystalline materials. *Comput Mater Sci* 77:81–92
- Paggi M, Wriggers P (2011) A nonlocal cohesive zone model for finite thickness interfaces. Part II: FE implementation and application to polycrystalline materials. *Comput Mater Sci* 50:1634–1643
- Rashid MF, Banerjee A (2013) Implementation and validation of a triaxiality dependent cohesive model: experiments and simulations. *Int J Fract* 181:227–239
- Rice JR (1968) A path independent integral and the approximate analysis of strain concentration by notches and cracks. *J Appl Mech* 15:379–386

- Rice JR (1980) The mechanics of earthquake rupture. In: Dziewonski AM, Boschi E (eds) *Physics of the earth's interior proceedings of international school of physics 'Enrico Fermi'*, Course 78, 1979. Italian Physical Society and North-Holland Publ Co, Amsterdam, pp 555–649
- Richards CW (1954) Size effect in the tension test of mild steel. *Proceedings of the American society for testing and materials* 54:995–1000
- Siegmund T, Brocks W (1999) Prediction of the work of separation in ductile failure and implications to the modeling of ductile failure. *Int J Fract* 99:97–116
- Siegmund T, Brocks W (2000) A numerical study on the correlation between the work of separation and the dissipation rate in ductile fracture. *Eng Fract Mech* 67:139–154
- Scheider I (2009) Derivation of separation laws for cohesive models in the course of ductile fracture. *Eng Fract Mech* 76:1450–1459
- Scheider I, Brocks W (2003) Simulation of cup-cone fracture using the cohesive model. *Eng Fract Mech* 70:1943–1961
- Sonmez FO, Demir A (2007) Analytical relations between hardness and strain for cold formed parts. *J Mater Process Technol* 186:163–173
- Sumpter JDG (2004) The energy dissipation rate approach to tearing instability. *Eng Fract Mech* 71:17–37
- Tada H, Paris P, Irwin G (1963) *The stress analyses of cracks handbook*. Paris Productions Incorporated (and Del Research Corporation), St. Louis, p 542
- Tvergaard V, Needleman A (1984) Analysis of the cup-cone fracture in a round tensile bar. *Acta Metall* 32:57–169
- Tvergaard V (1990) Effect of fiber debonding in a whisker-reinforced metal. *Mater Sci Eng A* 107:23–40
- Tvergaard V, Hutchinson JW (1992) The relation between crack growth resistance and fracture process parameters in elastic-plastic solids. *J Mech Phys Solids* 40:1377–1397
- Xu X, Needleman A (1994) Numerical simulations of fast crack growth in brittle solids. *J Mech Phys Solids* 42:1397–1434
- Yalcinkaya T, Cocks A (2015) Physics based formulation of a cohesive zone model for ductile fracture. *Key Eng Mater* 651–653:993–999
- Zhang ZL, Thaulow C, Ødegård J (2000) A complete Gurson model approach for ductile fracture. *Eng Fract Mech* 67:155–168
- Zienkiewicz OC, Taylor RL (2000) *The finite element method*, 5th edn. Butterworth-Heinemann, Oxford